Int. J. Electrochem. Sci., 16 **(2021)** Article ID: 210927, doi: 10.20964/2021.09.38

International Journal of
ELECTROCHEMICAL
SCIENCE
www.electrochemsci.org

TM(TM=Fe, Co, Ni)/N/O tri-doped Graphene Heterogeneous Electrocatalysts for Oxygen Reduction Reaction: A Theoretical Insight

L. B. Yu, J. Wu, Q. Y. Huang, S. S. Liu, L. Yang[*]

School of Energy and Power Engineering, Jiangsu University of Science and Technology, Zhenjiang, 212003, China
[*]E-mail: yljust18@163.com

Received: 15 May 2021 / *Accepted:* 6 July 2021 / *Published:* 10 August 2021

Density functional theory (DFT) is utilized to compute the thermodynamic free energy changes of the elementary reaction steps of the oxygen reduction reaction (ORR) on TMO_xN_{4-x} (TM=Fe, Co and Ni; x= 1-3) single atom catalysts (TMO_xN_{4-x}-SACs). Based on thermodynamic stability and catalytic ORR activity, it is found that CoO_xN_{4-x}-SACs show relatively good stability and activity. Furthermore, the final reduction reaction step ($OH^* + H^+ + e^- \rightarrow H_2O + *$) with the largest ΔG value towards five different CoO_xN_{4-x}-SACs is the potential-determining step (PDS). All calculated results suggest that the theoretical overpotential of CoO_2N_2-opp is munch close to that of Pt (111), implying the optimal electrocatalytic ORR activity among TMO_xN_{4-x}-SACs. Furthermore, electronic structure analysis reveals that the *d*-band center of Co for CoO_2N_2-opp is located rather far away from the Fermi level (set as zero) and binding states of adsorbed are reduced and the antibinding states of adsorbed OH* fragments are increased, compared with that of other CoO_xN_{4-x}-SACs. In conclusion, the introduction of N and O can effectively modify *d*-band of active metal center and adsorption of oxygen-contained intermediates, thus tune ORR activity.

Keywords: density functional theory, oxygen reduction reaction, single atom catalysts

1. INTRODUCTION

The massive depletion of fossil fuel has generated global energy consumption and serious environmental damage[1, 2]. Taking advantage of sustainable and renewable energy sources for fossil fuel grasps the crux to disposing of these related issues but desires highly efficient energy transformation and storge devices, particularly proton exchange membrane fuel cells (PEMFC), which depend heavily on oxygen reduction reaction (ORR) electrocatalysts to a great extent as they are the core of such energy

devices[3, 4]. Precious metal-based materials (e.g. platinum and its alloys) have been developed rapidly and are the most advanced ORR catalysts[5, 6]; however, their scarcity and consequent huge cost and poor long-term durability have greatly imposed restrictions on their extensive mercantile adhibition[7, 8]. Hence, developing cost effective electrocatalysts with outstanding performance is of great urgence on superseding expensive precious metal-based materials for ORR.

Single-atom catalysts (SACs), the most active frontiers in field of diversified catalysis, especially have been thought to be one of the most prospective substitutes for ORR, which have been ascribe to the maximum atomic utilization efficiency and adjustable electronic properties[9, 10]. The coordination configurations between active metal atoms and non-metal heteroatoms in the carbon-based materials, especially these TMN_x architectures (TM = Mn, Fe, Co, Ni, etc.), can effectively regulate the electronic structure of transition metal hosts and thereby optimize the binding affinity to oxygenated intermediates, contributing to a superior activity[7, 9]. Consequently, by means of modifying the local electronic properties of active centers, corresponding electrocatalytic performances can be considerably modulated. Numerous studies have demonstrated that such catalysts with single metallic cofactors can be further enhanced by introducing alien atoms (e.g. B, P, S) in the active architectures to form new atomistic coordination structures[11-14]. For instance, Wang et al. reported that constructed the B, N co-coordinated Zn-B/N-C catalysts can render adequate delocalized electrons to originate moderate binding strength for oxygenated reaction fragments and afterwards demonstrate remarkable capacity for catalyzing ORR[11]. Yuan's group studied how N and P atoms dual-coordinated Fe (named as Fe-N/P-C) prepared via high-temperature pyrolysis method act as actives motifs for catalyzing ORR in acidic media[12]. Besides, Zhang and co-workers successfully synthesized three different single metal (Fe, Co and Ni) elements embedded in porous N, S-codoped carbon (NSC) based materials and surveyed the effect of sulfuration on ORR activity of these samples[13]. The aforementioned researches show that the catalysts with various bindings between the B, P or S elements and the TMN_x centers present fairly good ORR performance, deriving from the different electronegativity and atomic radius from B, P or S element to N element.

It is worth noting that the presence of oxygen function groups (e.g. hydroxyl, ketone, ester) in the graphene are inevitable, even after high-temperature annealing or chemical reduction[15]. Moreover, the introduction of oxygen elements could also be conducted through manufacturing holes via utilizing electrons or ions[15]. Consequently, doping O atom has also been used to adjust the electronic properties of electrocatalysts and alter corresponding electrocatalytic activity and selectivity of reactions. In this respect, Dong et al. determined that the synergistic effect of O and N dopants promote the activation of oxygen-containing intermediates and thus enhance electrocatalytic activity of the single-doped samples[16]. Supporting this in the different systems, Yang et al. successfully prepared catalysts that O and N elements co-coordinated Mn active centers atomically dispersed in the graphene framework and these samples exhibit superior performance for ORR[17]. Similarly, Tang et al. found that as-synthesized Co/N/O tri-doped graphene catalysts via defect engineering strategy effectively accelerate oxygen electrocatalysis kinetics[18]. However, current cutting edge characterization techniques cannot characterize these corresponding unique structures. On the other hand, the investigation of the formation mechanism for the different coordination structures and the conclusive correlation between the single metallic center affected by introducing O and N atoms and catalytic performances are also challenging.

Fortunately, the crown ether configuration is manually incorporated into graphene, which provide a simple coordination environment for theoretical stimulation[15]. Inspired by aforementioned information, it is necessary to construct a series of relevant dual-N,O coordinated single metal atoms catalysts and systematically investigate the relationship between the orientation of the doping O and N elements for the SACs and corresponding ORR activity.

In this manuscript, three kinds of TMO_xN_{4-x}-SACs (TM = Fe, Co, Ni; x = 1-3) are constructed via altering the doping content as well as coordination configurations of O and N atoms. The spin-polarized density functional theory (DFT) calculations are used to systematically investigate the geometric structure and further examine ORR electrocatalysis. The TMO_xN_{4-x} (x = 1-3) represents the TM atom bonded with N and O atoms and the atomic configurations are schematically shown in Figure 1.

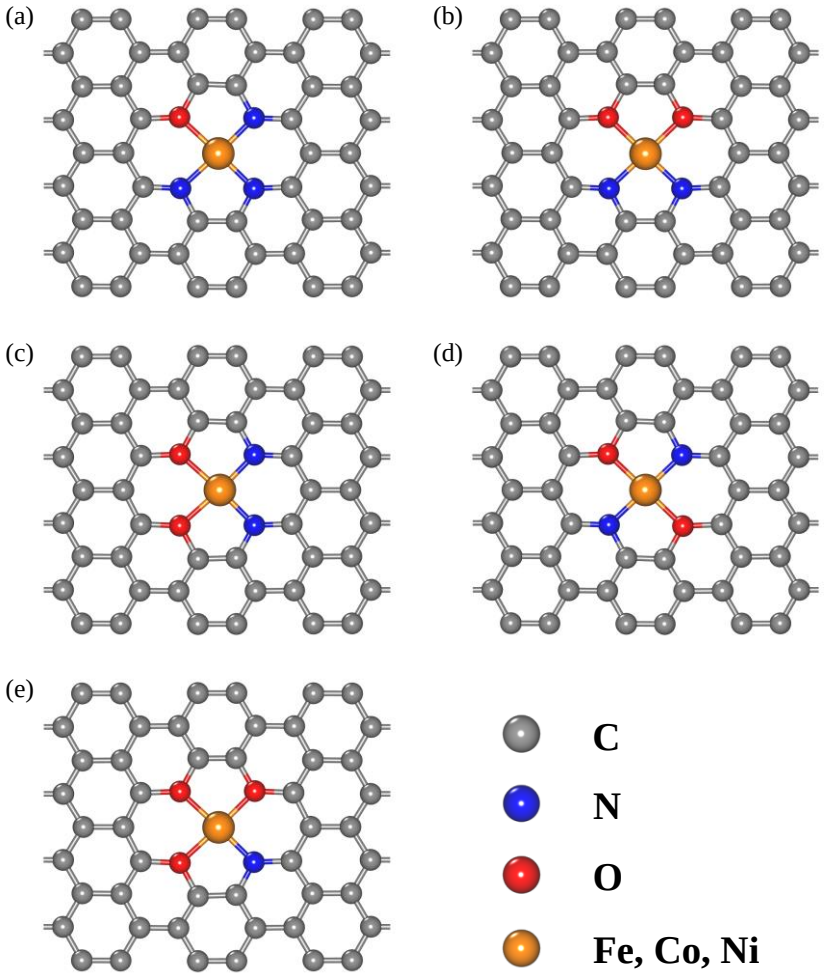

Figure 1. The optimal geometry structures of (a) TMO_1N_3, (b) TMO_2N_2-pen, (c) TMO_2N_2-hex, (d) TMO_2N_2-opp, (e) TMO_3N_1 embedded graphene (TM = Fe, Co, Ni).

Among them, three TMN_2O_2 structures are specifically defined according to the relative positions of O atoms, where the O atoms in pen or hex configuration are located in the same pentatomic or hexatomic ring (named as TMN_2O_2-pen and TMN_2O_2-hex, respectively) while in the opp model

(TMN_2O_2-opp), they are located on a diagonal line in opposite directions with reference to the position of the metal atom. Based on the constructed models, our results indicate that CoO_2N_2-opp exhibit remarkable electrocatalytic activity, in line with previous experimental results.

2. COMPUTATIONAL METHOD

The spin-polarized total energy calculations are performed using the Dmol^3 in Materials Studio software package[15]. The generalized-gradient approximation (GGA) in the form of the Perdew-Burke-Ernzerhof (PBE) functional is adopted to deal with the exchange-correlation energy[19]. The weak interactions between the intermediates and catalysts are is described by the DFT-D2 in Grimme's scheme[20]. The spin-unrestricted method is used for all calculations[15]. The density functional theory (DFT) Semi-core Pseudopotentials (DSPP) are employed to replace the core electrons for reducing the computational cost and the double numerical atomic orbital augmented by a polarization function (DNP) is chosen as the basis set[21]. A smearing value of 0.005 Ha (1 Ha = 27.21 eV) is specified for the orbit occupation to speed up convergence. During the structural geometry optimization, the convergence criteria are set as 1×10^{-5} Ha for energy, 0.002 Ha/Å for maximum force, and 0.005 Å for displacement. The conductor-like screening model (COSMO) was used to simulate a H_2O solvent environment for all calculations. The dielectric constant is set as 78.54 for H_2O. The (5×4) supercell is adopted with 15 Å vacuum to avoid the artificial interactions between the catalyst and its images. During the geometrical optimization, the systems are free to relax.

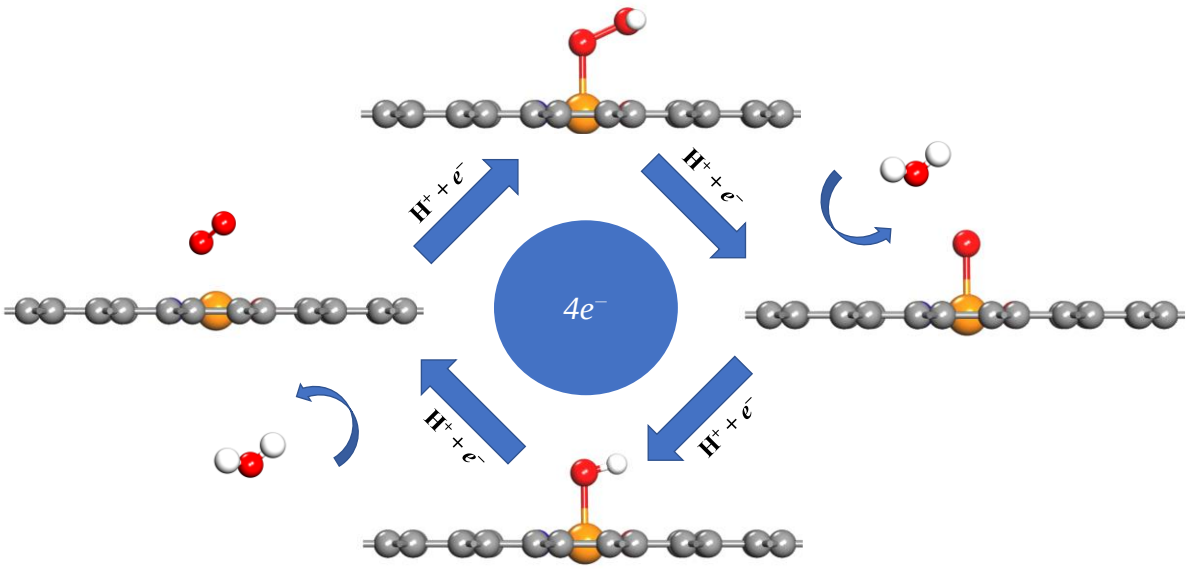

Figure 2. Schematics of the $4e^-$ reduction process of the ORR catalyzed on all TMO_xN_{4-x}-SACs.

As we can see in Figure 2, all oxygen-contained intermediates for ORR are described as proton/electron ($H^+ + e^-$) transfers. In this work, the ORR is assumed to proceed by $4e^-$ reduction process[22], which compared of the following basic reaction steps:

OOH formation: $O_2(g) + * + (H^+ + e^-) \rightarrow OOH*$ (1)

O formation: $OOH* + (H^+ + e^-) \rightarrow O* + H_2O(l)$ (2)

OH formation: $O* + H_2O(l) + (H^+ + e^-) \rightarrow OH* + H_2O(l)$ (3)

H_2O formation: $OH* + H_2O(l) + (H^+ + e^-) \rightarrow 2H_2O(l) + *$ (4)

where * denotes as an adsorption site on the catalytic surface, (g) and (l) refer to gas and liquid phase, respectively.

The binding energy (E_b), cohesive energy (E_{coh}) and formation energy (E_f) of TMO_xN_{4-x} embedded graphene are calculated by using following formulae:

$$E_b = E_{TMOxN4-x} - (E_{support} + E_{TM}) \quad (5)$$

$$E_{coh} = E_{bulk}/n - E_{TM} \quad (6)$$

$$E_f = E_{TMOxN4-x} + 6 \times E_C - (E_{graphene} + E_{TM} + xE_O + (4-x) \times E_N) \quad (7)$$

where $E_{TMOxN4-x}$, $E_{support}$, $E_{graphene}$, E_{coh} and E_{TM} denote the total energies of TMN_xO_{4-x} embedded graphene, catalyst monolayer without TM decoration, perfect graphene, bulk TM metal and the corresponding atomic TM, respectively. E_C, E_N and E_O are the average total energies of a single C atom in perfect graphene, a single N atom in N_2 and a single O atom in O_2, respectively. n is the number of TM atoms in the corresponding cell. x (= 1-3) is the number of substituted N atoms or doped O atoms when generating the TMO_xN_{4-x} embedded graphene from the TMN_4 embedded graphene.

The adsorption energies E_{ad} of the ORR intermediates are calculated by:

$$E_{ad} = E_{system} - (E_{catalyst} + E_M) \quad (8)$$

where E_{system} and E_M stand for the total energy of adsorbed catalysts and ORR O-contained intermediates, respectively.

The computational hydrogen electrode (CHE) model proposed by Nørskov et al. is used to compute the Gibbs free energy change (ΔG) of each elementary step of the ORR[23]. In this model, the chemical potential of $H^+ + e^- \rightarrow 1/2H_2$ under standard conditions is set to be at equilibrium with 0 V relative to the standard hydrogen electrode (SHE). The ΔG of each elementary step is determined by

$$\Delta G = \Delta E + \Delta ZPE - T\Delta S + \Delta G_U + \Delta G_{pH} \quad (9)$$

where ΔE is the electronic energy difference directly obtained from DFT calculation, ΔZPE represents the change of zero-point energy (ZPE), and $T\Delta S$ is the change in entropy at 298.15 K. The ZPE and entropies of ORR intermediates are calculated based on the vibrational frequencies. $\Delta G_U = -eU$, wherein U is the potential related to the standard hydrogen electrode, and $\Delta G_{pH} = -k_B T \ln 10 \times pH$. In this work, the pH of the solution is assumed to be zero for an acid medium and the free energy contribution caused by changing the H concentration is neglected. Since the DFT method failed to accurately describe the high-spin ground state of O_2 molecule, the Gibbs free energy of O_2 (G_{O2}) is obtained by $G_{O2}(g) = 4.92 + 2G_{H2O(l)} - 2G_{H2(g)}$ by utilizing OER equilibrium under standard conditions[24]. The thermodynamic activity of the ORR can be visualized by investigating the overpotential(η), which is determined by:

$$\eta = 1.23 + \max\{\Delta G_1, \Delta G_2, \Delta G_3, \Delta G_4\}/e \quad (9)$$

where ΔG_n (n = 1-4) denotes as the free energy changes of corresponding electrochemical ORR steps. Noteworthy, the negative ΔG value corresponds to an exothermic adsorption process, indicating the spontaneity characteristic. On the basis of this definition, the lower the value of overpotential, the better the catalytic performance of the corresponding electrocatalysts.

3. RESULTS AND DISCUSSION

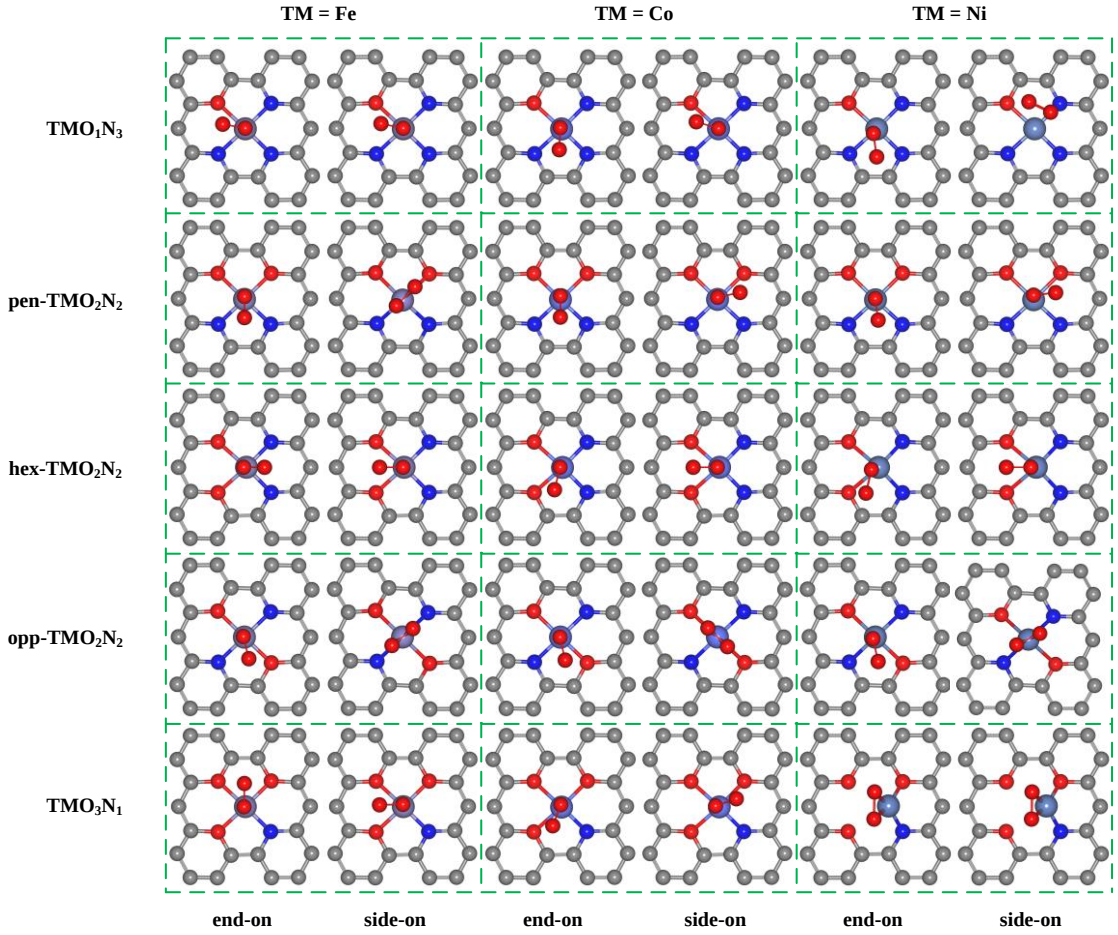

Figure 3. The optimal adsorption structure of O_2 molecule on all TMO_xN_{4-x}-SACs.

Before exploring the whole ORR catalytic processes, we firstly research the geometry structure and thermodynamic stability of TMO_xN_{4-x}-SACs. The calculated of binding energies E_b and formation energies E_f are shown as in Figure 4(a). It is well-known that the value of E_b is less than that of E_{coh}, meaning that the binding of metal atoms on O, N-codped graphene is energetically more favorable than the metal aggregation[25]. Therefore, the smaller E_b values of TMO_1N_3, TMO_2N_2 display good capacity of resisting against the atomic aggregation, compared with the bulk cohesive energy[21]. The exception of TMO_3N_1 are ascribe to the faint TM-N bonds. Therefore, the increasing in the number of TM-O bonds would decrease the binding strength between the TM atom and its supports. Moreover, the formation energies E_f are calculated to evaluate the difficulty for synthesis of these TMO_xN_{4-x}-SACs. As displayed in Figure 4(a), TMO_xN_{4-x}-SACs present rather the negative formation energies, indicating the possibility to readily fabricate them. Therefore, these catalysts are promising to be synthesized in the laboratory without much energy cost. Overall, TMO_1N_3 and TMO_2N_2 samples can offer good thermodynamic stability, compared to TMO_3N_1 samples.

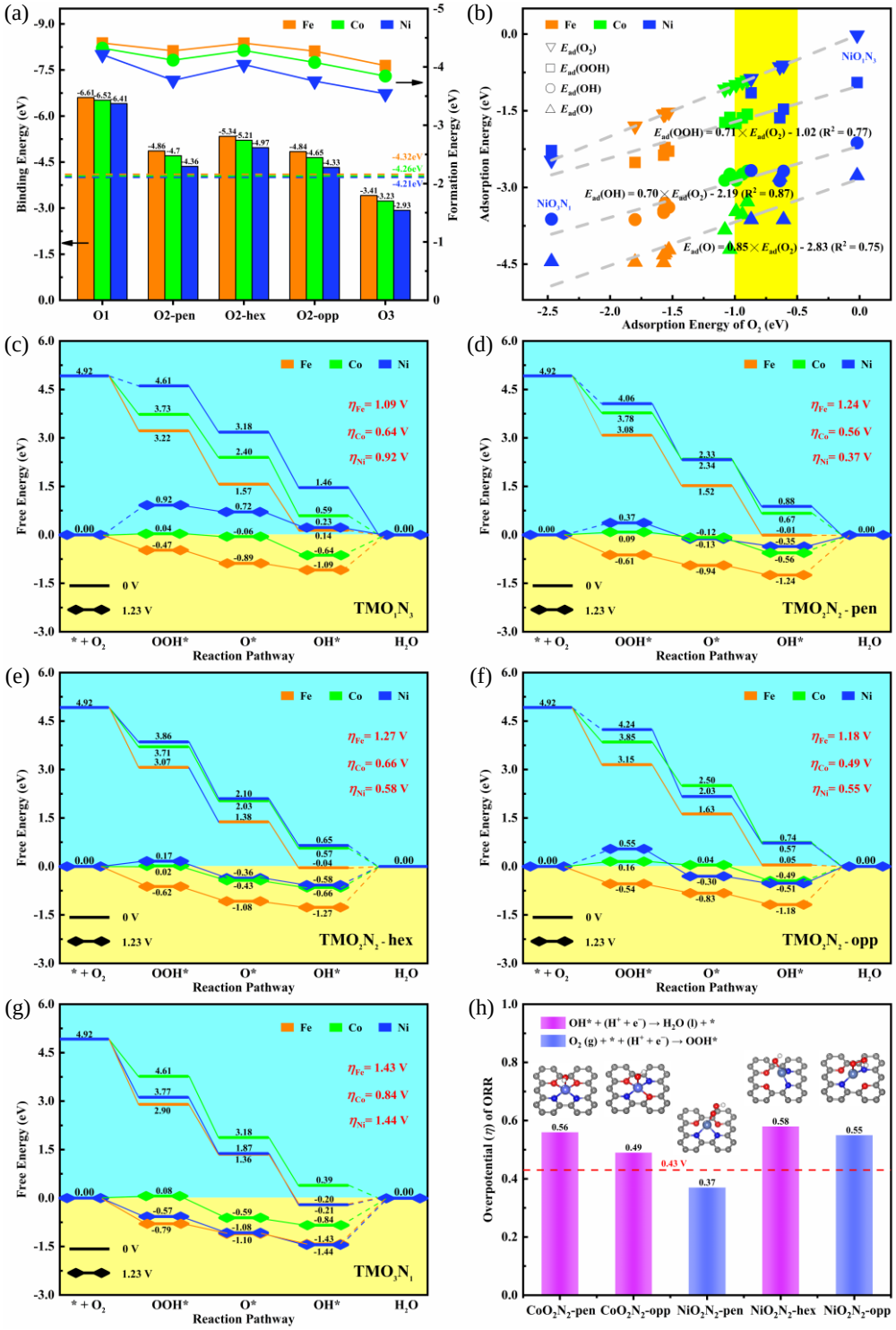

Figure 4. Thermodynamic analysis. (a) The thermodynamic stability (for E_b) and experimental feasibility (for E_f) and three dash lines represent corresponding TM cohesive energy. (b) The adsorption energy E_{ad} of oxygen-contained intermediates as a function of $E_{ad}(O_2)$. (c-g) The ORR free energy diagram under 0 and 1.23 V. The G for the reaction species is labeled in the profiles, and the potential-determined steps (PDS) of the elementary reaction is highlighted in dotted line. (h) Calculated theoretical ORR overpotential on highly active systems and corresponding theoretical model related to PDS.

With regard to the reaction process is originated from the protonation of oxygen molecules (O_2) in the first step, we firstly study the adsorption ability of TMO_xN_{4-x}-SACs towards O_2. In this regard, we chiefly focus on the adsorption strength of O_2 on the TM active sites of TMO_xN_{4-x}-SACs. By comparing the corresponding adsorption energy of O_2 (see in Table 1), we find that TMO_xN_{4-x} configurations can effectively promote the activation of O_2 except for the case of NiO_1N_3.

Table 1. The adsorption energy (E_{O2}) of O_2 on TMO_xN_{4-x}-SACs and the O=O bond length (L_{O-O}) of the adsorbed O_2. ($E_{ad(O2)}$ in eV, L_{O-O} in Å)

Model	Type	$E_{ad(O2)}$	L_{O-O}	Model	Type	$E_{ad(O2)}$	L_{O-O}	Model	Type	$E_{ad(O2)}$	L_{O-O}
FeO_1N_3	end-on	-1.56	1.33	CoO_1N_3	end-on	-1.11	1.31	NiO_1N_3	end-on	-0.02	1.30
	side-on	-1.51	1.33		side-on	-0.99	1.32		side-on	0.13	1.29
FeO_2N_2-pen	end-on	-1.57	1.33	CoO_2N_2-pen	end-on	-0.94	1.32	NiO_2N_2-pen	end-on	-0.61	1.30
	side-on	-1.37	1.40		side-on	-0.84	1.33		side-on	-0.63	1.30
FeO_2N_2-hex	end-on	-1.57	1.33	CoO_2N_2-hex	end-on	-1.08	1.32	NiO_2N_2-hex	end-on	-0.64	1.32
	side-on	-1.58	1.33		side-on	-1.00	1.33		side-on	-0.62	1.32
FeO_2N_2-opp	end-on	-1.53	1.33	CoO_2N_2-opp	end-on	-0.90	1.33	NiO_2N_2-opp	end-on	-0.87	1.31
	side-on	-1.36	1.41		side-on	-0.91	1.40		side-on	-0.84	1.31
FeO_3N_1	end-on	-1.80	1.33	CoO_3N_1	end-on	-1.04	1.32	NiO_3N_1	end-on	-2.47	1.41
	side-on	-1.73	1.34		side-on	-0.97	1.33		side-on	-2.47	1.41

For compensation, the adsorbed O_2 shows a stretched O=O bond length compared to that of the free O_2 (L_{O-O} = 1.22Å)[6] on account of the strong binding strength between the oxygen atoms and the transition metal hosts. All optimized adsorption configurations of O_2 on TMO_xN_{4-x}-SACs are displayed in Figure 3. Combined with the corresponding adsorption energy (see in Table 1), it is clearly observed that the O_2 is adsorbed on TMO_xN_{4-x} with end-on except for NiO_1N_3, while NiO_3N_1 incline to adsorb the O_2 with side-on model. It is well-known that the O_2 is firstly protonated by assimilating an electron and hydrion transferred, then forming orderly O-contained reaction intermediates adsorbed on top site of the metal atom (as illustrated in Figure 2). Here, their adsorption energies (see Table 2) are plotted as a function of O_2 adsorption energy, as presented in Figure 4(b).

Table 2. The adsorption energies of O_2, OOH, O, OH on TMO_xN_{4-x}-SACs (E_{ad} in eV).

Model	$E_{ad(O2)}$	$E_{ad(OOH)}$	$E_{ad(O)}$	$E_{ad(OH)}$
FeO_1N_3	-1.56	-2.22	-4.28	-3.31
FeO_2N_2-pen	-1.57	-2.37	-4.32	-3.45

FeO_2N_2-hex	-1.57	-2.37	-4.47	-3.49
FeO_2N_2-opp	-1.53	-2.29	-4.22	-3.39
FeO_3N_1	-1.80	-2.51	-4.46	-3.63
CoO_1N_3	-0.99	-1.75	-3.47	-2.86
CoO_2N_2-pen	-0.94	-1.64	-3.53	-2.74
CoO_2N_2-hex	-1.08	-1.73	-3.83	-2.86
CoO_2N_2-opp	-0.90	-1.57	-3.28	-2.68
CoO_3N_1	-1.04	-1.63	-4.21	-2.90
NiO_1N_3	-0.02	-0.95	-2.77	-2.13
NiO_2N_2-pen	-0.61	-1.47	-3.63	-2.68
NiO_2N_2-hex	-0.64	-1.64	-2.80	-2.87
NiO_2N_2-opp	-0.87	-1.15	-3.63	-2.67
NiO_3N_1	-2.47	-2.28	-4.45	-3.62

The calculated results suggest that their adsorption energies decrease in a certain range: O* > OH* > OOH* > O_2* on these TMO_xN_{4-x}-SACs. Moreover, the universal linear relationships between the ORR intermediates are clearly observed, which is ascribed to the similar TM-O binding[21, 26]. Therefore, a relatively stronger (or weaker) adsorption energy of O_2 can reveal that the other three oxygen-containing fragments also show the stronger (or weaker) binding capacity on the same active site, suggesting that O_2 adsorption energy could be used as an activity parameter to roughly forecast the activity of these TMO_xN_{4-x}-SACs with same active sites. According to Sabatier's principle[19, 27, 28], the adsorption affinity of oxygen-contained intermediate products on any one of ORR catalysts should be neither too strong nor too weak, because a weak binding effect of oxygen with active sites is incapable of guaranteeing an adequate protonation of the O_2, whereas a strong binding strength between oxygen and catalysts could give rise to the difficulty to dissociation of a water molecule. In these two special situations, the associated overpotential is unavoidably very high. By comparison, the O_2 is mildly activated on CoO_2N_2-pen ($E_{ad(O2)}$ = -0.94 eV), CoO_2N_2-opp ($E_{ad(O2)}$ = -0.9 eV), NiO_2N_2-pen ($E_{ad(O2)}$ = -0.61 eV) NiO_2N_2-hex ($E_{ad(O2)}$ = -0.64 eV) and NiO_2N_2-opp ($E_{ad(O2)}$ = -0.84 eV) SACs, which could promote the subsequent reduction of O_2 molecules.

To obtain an underlying comprehending on the catalytic ability of TMO_xN_{4-x}-SACs towards ORR, we further examine the thermodynamic performances of ORR by calculating the free energy changes ΔG of all reaction steps (see Table 3). Calculated results demonstrate that the formation of OOH* on most TMO_xN_{4-x}-SACs is energetically favorable with a negative free energy change at zero potential. Particularly, O_2 molecules are excessively activated with rather large values of ΔG ranged from -2.02 to -1.70 eV in FeO_xN_{4-x}-SACs systems. In particular, the CoO_2N_2-opp show a moderate ΔG of -1.07 eV for the OOH* fragments as O_2 molecules are activated on this sample.

Table 3. The Gibbs free energies of OOH, O, OH on TMO_xN_{4-x}-SACs and the free energy change (ΔG) of the elementary steps along the reaction path at 0 V. (G, ΔG in eV).

Model	G_{OOH}	G_O	G_{OH}	ΔG_1	ΔG_2	ΔG_3	ΔG_4
FeO_1N_3	3.22	1.57	0.14	-1.70	-1.65	-1.43	-0.14
pen-FeO_2N_2	3.08	1.52	-0.01	-1.84	-1.56	-1.53	0.01

hex-FeO_2N_2	3.07	1.38	-0.04	-1.85	-1.68	-1.42	0.04
opp-FeO_2N_2	3.15	1.63	-0.05	-1.77	-1.53	-1.58	-0.05
FeO_3N_1	2.90	1.36	-0.20	-2.02	-1.54	-1.56	0.20
CoO_1N_3	3.73	2.40	0.59	-1.19	-1.32	-1.81	-0.59
pen-CoO_2N_2	3.78	2.34	0.67	-1.14	-1.43	-1.68	-0.67
hex-CoO_2N_2	3.71	2.03	0.57	-1.21	-1.67	-1.46	-0.57
opp-CoO_2N_2	3.85	2.50	0.74	-1.07	-1.35	-1.76	-0.74
CoO_3N_1	3.77	1.87	0.39	-1.15	-1.90	-1.48	-0.39
NiO_1N_3	4.61	3.18	1.46	-0.31	-1.43	-1.72	-1.46
pen-NiO_2N_2	4.06	2.33	0.88	-0.86	-1.73	-1.44	-0.88
hex-NiO_2N_2	3.86	2.10	0.65	-1.06	-1.76	-1.45	-0.65
opp-NiO_2N_2	4.24	2.16	0.72	-0.68	-2.07	-1.44	-0.72
NiO_3N_1	3.12	1.38	-0.21	-1.80	-1.74	-1.58	0.21

The same phenomenon is also observed in three NiO_2N_2-SACs systems. In contrast, NiO_1N_3 show a relatively small value of ΔG (-0.31 eV) to generate OOH* species owing to their relatively inert interactions with O_2 molecules. Subsequently, it is found that the formation of O* and H_2O is exothermic for all the tested TMO_xN_{4-x}-SACs systems with rather large ΔG ranged from -2.07 to -1.32 eV, indicating that they will easily react with second electron/proton pair to form an O* fragment and dissociate a H_2O molecule. According to larger negative ΔG of -1.76 to -1.42 eV, it is distinctly observed that the naked O* fragments can be easily hydrogenated to generate OH* fragments. For the last step, all the TMO_xN_{4-x}-SACs systems can react to the fourth proton-electron pair to promote the dissociation of the second H_2O molecule except for the case of FeO_2N_2-pen, FeO_2N_2-hex, FeO_3N_1 and NiO_3N_1, which show positive value of ΔG ranged from 0.01 to 0.21 eV. That is because their stronger interactions the OH* fragments, causing the hydrogenation of OH* energetically unfavorable. Ideally, the overall ORR steps should generate 1.23 V per electron to ensure that the free energy change of each elementary step is zero at equilibrium potential of 1.23 V, revealing the existence of potential-determining step (PDS) and overpotential (η). As shown in Figure 4(c-g), the PDS of FeO_xN_{4-x} and CoO_xN_{4-x} systems is the conversion of OH* to H_2O.

Table 4. The Mulliken charge analysis of CoOxN4-x-SACs (Q in e). The negative and positive values of Q stand for charge the accumulation and depletion.

	CoO_1N_3	CoO_2N_2-pen	CoO_2N_2-hex	CoO_2N_2-hex	CoO_3N_1
Q(Co)	0.283	0.269	0.310	0.214	0.385
Q(OH*)	-0.338	-0.316	-0.348	-0.313	-0.350

However, it is worth noting that NiO_xN_{4-x}-SACs show multiple PDS, wherein the PDS of NiO_1N_3, NiO_2N_2-pen and NiO_2N_2-opp become the first step ($O_2 \rightarrow$ OOH*) whereas the PDS of NiO_2N_2-hex and

NiO_3N_1 is consistent with that of FeO_XN_{4-X}-SACs and CoO_XN_{4-X} systems. Figure 4(h) displays the η of TMO_XN_{4-X}-SACs with relatively good ORR activity. As we can see, the η of CoO_2N_2-pen, CoO_2N_2-opp, NiO_2N_2-pen, NiO_2N_2-hex and NiO_2N_2-opp are 0.56, 0.49, 0.37, 0.58 and 0.55 V, respectively. However, the structures of three NiO_2N_2-SACs is found to be collapsed after the adsorption of O-contained intermediates, implying that they have poor stability against oxidation. Therefore, these three NiO_2N_2-SACs are not considered as outstanding electrocatalysts regardless of excellent ORR activity. Remarkably, the η (=0.49 V) of CoO_2N_2-opp is comparable to that of Pt (0.43 V)[27], implying the superior catalytic ORR performance of the CoO_2N_2-opp sample, which is in perfect agreement with the experimental results[18].

We have evaluated the above three types of TMO_xN_{4-x}-SACs from the thermodynamic aspect. It is found that the ORR activity of CoO_xN_{4-x}-SACs is better than that of FeO_xN_{4-x} samples and the stability of CoO_xN_{4-x}-SACs is far superior to that of NiO_xN_{4-x} samples.

For the sake of revealing the synergistic influence of N and O on the activity of metal center, CoO_xN_{4-x}-SACs are taken as examples to carry out relevant electronic analysis, involving the Mulliken Charge Distribution (Q) listed in Table 4, OH* adsorption energy, *d*-band center and overpotential shown in Figure 5(a) and the partial density of states (PDOS) of OH* shown in Figure 5(b). The poisoning phenomenon (OH* → H_2O) of CoO_xN_{4-x}-SACs and the good liner relationship (see Figure 4(b)) reveal that the adsorption energy of OH* also can be used as a representative to study the connection between adsorption energy of O-contained intermediates and ORR activity.

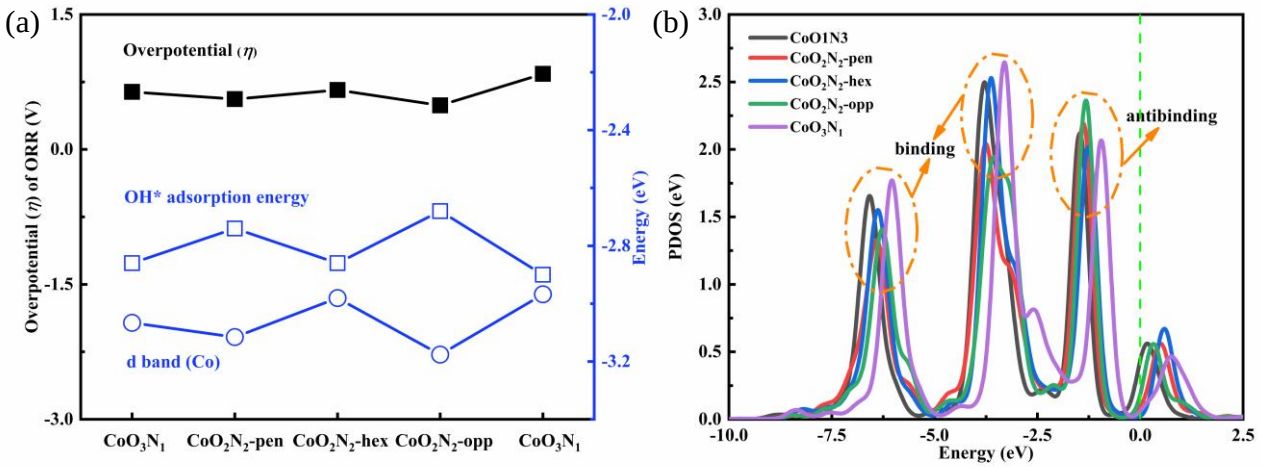

Figure 5. Electron analysis. (a) The *d*-band center of Co, adsorption energy of OH and overpotential of ORR on the CoO_xN_{4-x}-SACs. (b) the partial density of states (PDOS) of OH* fragments.

As shown in Figure 5(a), the lower adsorption energy of OH shows that the *d*-band center of Co is located rather far away from the Fermi level, suggesting that the corresponding electrocatalysts is not conducive to the adsorption of OH and exhibit more outstanding ORR activity with a lower overpotential. In addition, the Mulliken charges display that the OH* specie adsorbed on the CoO_2N_2-opp sample has a negatively charged of -0.313 e whereas the metal center is positively charged by 0.214 e, indicating the relatively weak Co-OH binding effect. On CoO_1N_3, CoO_2N_2-pen, CoO_2N_2-hex and CoO_3N_1, the OH*

species obtains more electrons compared with CoO_2N_2-opp, leading to the comparatively strong interaction between Co and OH* fragments. Figure 5(b) further unveil the underlying mechanism of the electron-mediated adsorption by the PDOS of OH*, revealing that the binding states are enhanced and the antibinding states are reduced for CoO_1N_3, CoO_2N_2-pen, CoO_2N_2-hex and CoO_3N_1. Conversely, the binding states are reduced and the antibinding states are increased for CoO_2N_2-opp. Therefore, the Mulliken Charge Distribution and PDOS clearly explains the different changes of the OH adsorption caused by the synergistic effect of N and O atoms. As a consequence, the activity of metal center for ORR can be effectively tuned by the collaborative effect of N and O doping.

4. CONCLUSIONS

In this manuscript, the stability and ORR activities of TMOxN4-x-SACs (TM= Fe, Co and Ni) catalysts are theoretically investigated. It can be concluded that TMO_1N_3 and TMO_2N_2 samples can offer good thermodynamic stability compared with TMO_3N_1 systems. Interestingly, the CoO_2N_2-pen, CoO_2N_2-opp, NiO_2N_2-pen, NiO_2N_2-hex and NiO_2N_2-opp show good catalytic ORR activity for ORR. However, the NiO_2N_2-pen, NiO_2N_2-hex and NiO_2N_2-opp catalysts is found to have poor stability against oxidation after the adsorption of O-contained intermediates, implying they are not considered as outstanding electrocatalysts. Remarkably, the theoretical overpotential of CoO_2N_2-opp is munch close to that of Pt(111), holding the best ORR activity compared of other TMOxN4-x-SACs. Our studies will inspire more theoretical and experimental researches on exploring potential single metal atom electrocatalysts for ORR.

CONFLICTS OF INTEREST
There are no conflicts to declare.

ACKNOWLEDGMENTS
We acknowledge the supports from the Postgraduate Research & Practice Innovation Program of Jiangsu Province (KYCX20_3160).

References

1. K. Hu, L. Tao, D. Liu, J. Huo and S. Wang, *ACS Appl. Mater. Inter*., 8 (2016) 19379.
2. J. Jia, Z. Chen, Y. Liu, Y. Li and J. Zhao, *ACS Appl. Mater. Inter*., 12 (2020) 54517.
3. W. Ni, Y. Gao, Y. Zhang, H.A. Younus, X. Guo, C. Ma, Y. Zhang, J. Duan, J. Zhang and S. Zhang, *ACS Appl. Mater. Inter*., 11 (2019) 45825.
4. J. Park, Z. Chen, R.A. Flores, G. Wallnerstrom, A. Kulkarni, J.K. Norskov, T.F. Jaramillo and Z. Bao, *ACS Appl. Mater. Inter.*, 12 (2020) 39074.
5. Y. Gao, Z. Cai, X. Wu, Z. Lv, P. Wu and C. Cai, *ACS Catal.*, 8 (2018) 10364.
6. J. Zhang, Z. Zhou, F. Wang, Y. Li and Y. Jing, *ACS Sustain. Chem. Eng*., 8 (2020) 7472.
7. W. Zhang, K. Mao and X.C. Zeng, *ACS Sustain. Chem. Eng.*, 7 (2019) 18711.
8. F. Li, G.F. Han, Y. Bu, H.J. Noh, J.P. Jeon, T.J. Shin, S.J. Kim, Y. Wu, H.Y. Jeong, Z. Fu, Y. Lu and J.B. Baek, *Angew. Chem. Int. Ed*., 59 (2020) 23678.

9. W. Qi, W. Huang, J. Niu, B. Zhang, Z. Zhang and W. Li, *Appl. Surf. Sci.*, 540 (2021) 148325.
10. Z. Lu, G. Xu, C. He, T. Wang, L. Yang, Z. Yang and D. Ma, *Carbon*, 84 (2015) 500.
11. J. Wang, H. Li, S. Liu, Y. Hu, J. Zhang, M. Xia, Y. Hou, J. Tse, J. Zhang and Y. Zhao, *Angew. Chem. Int. Ed*., 60 (2021) 181.
12. K. Yuan, D. Lutzenkirchen-Hecht, L. Li, L. Shuai, Y. Li, R. Cao, M. Qiu, X. Zhuang, M.K.H. Leung, Y. Chen and U. Scherf, *J. Am. Chem. Soc*., 142 (2020) 2404.
13. J. Zhang, Y. Zhao, C. Chen, Y.C. Huang, C.L. Dong, C.J. Chen, R.S. Liu, C. Wang, K. Yan, Y. Li and G. Wang, *J. Am. Chem. Soc*., 141 (2019) 20118.
14. X. Xu, X. Yan, Z. Zhong, L. Kang and J. Yao, *Carbon*, 145 (2019) 311.
15. B.B. Xiao, H.Y. Liu, L. Yang, E.H. Song, X.B. Jiang and Q. Jiang, *ACS Appl. Energ. Mater.*, 3 (2019) 260.
16. Y. Dong, M. Zhou, W. Tu, E. Zhu, Y. Chen, Y. Zhao, S. Liao, Y. Huang, Q. Chen and Y. Li, *Adv. Funct. Mater.*, 29 (2019) 1900015.
17. Y. Yang, K. Mao, S. Gao, H. Huang, G. Xia, Z. Lin, P. Jiang, C. Wang, H. Wang and Q. Chen, *Adv. Mater.*, 30 (2018) 1801732.
18. C. Tang, B. Wang, H.F. Wang and Q. Zhang, *Adv. Mater*., 29 (2017) 1703185.
19. X. Zhang, Z. Yang, Z. Lu and W. Wang, *Carbon*, 130 (2018) 112.
20. N. Mohammadi-Rad, M.D. Esrafili and J.J. Sardroodi, *J. Mol. Graph. Mod*., 96 (2020) 107537.
21. B.B. Xiao, L. Yang, H.Y. Liu, X.B. Jiang, B. Aleksandr, E.H. Song and Q. Jiang, *Appl. Surf. Sci.*, 537 (2020) 147846.
22. T. He, C. Zhang, G. Will and A. Du, *Catal. Tod*., 351 (2020) 113.
23. A. Kulkarni, S. Siahrostami, A. Patel and J.K. Norskov, *Chem. Rev*., 118 (2018) 2302.
24. M. Yin, Z.X. Dai, S.N. Chen, L.J. Dong, X.L. Zhang, Y.J. Xu and C.H. Sun, *J. Phys. Chem*. C, 124 (2020) 13283.
25. L. Li, R. Huang, X. Cao and Y. Wen, *J. Mater. Chem.* A, 8 (2020) 19319.
26. B.B. Xiao, H.Y. Liu, X.B. Jiang, Z.D. Yu and Q. Jiang, *RSC Advances*, 7 (2017) 54332.
27. Z. Xue, X. Zhang, J. Qin and R. Liu, *J. Energ. Chem*., 55 (2021) 437.
28. M. Hu, S. Li, S. Zheng, X. Liang, J. Zheng and F. Pan, *J. Phys. Chem.* C, 124 (2020) 13168.